



Article

Role of Defects and Radiation Damage on He Diffusion in Magnetite: Implication for (U-Th)/He Thermochronology

Fadel Bassal ¹, Jérôme Roques ¹, Marianna Corre ², Fabrice Brunet ², Richard Ketcham ³ , Stéphane Schwartz ² , Laurent Tassan-Got ¹ and Cécile Gautheron ^{4,*}

¹ IJCLab, Université Paris-Saclay, CNRS/IN2P3, 91405 Orsay, France; fadel.bassal@live.fr (F.B.); jerome.roques@universite-paris-saclay.fr (J.R.); tassango@ijclab.in2p3.fr (L.T.-G.)

² ISTERre, Université Grenoble Alpes, Université Savoie Mont Blanc, CNRS, IRD, Université Gustave Eiffel, 38000 Grenoble, France; marianna.corre@univ-grenoble-alpes.fr (M.C.); fabrice.brunet@univ-grenoble-alpes.fr (F.B.); stephane.schwartz@univ-grenoble-alpes.fr (S.S.)

³ Jackson School of Geosciences, The University of Texas at Austin, Austin, TX 78712, USA; ketcham@jsg.utexas.edu

⁴ Geosciences Paris Saclay (GEOPS), Université Paris Saclay, 91404 Orsay, France

* Correspondence: cecile.gautheron@universite-paris-saclay.fr

Abstract: The discovery of He retentivity in magnetite has opened up the use of the magnetite (U-Th)/He method as a thermochronometer to date the exhumation of mafic and ultramafic rocks, and also as a chronometer to date magnetite crystallization during serpentinization. However, published He diffusion data reveal more complex behavior than expected. To resolve this issue and generalize the understanding of He retention in magnetite, we conducted a multiscale theoretical study. We investigated the impact of natural point-defects (i.e., vacancies unrelated to radiation damage) and defects associated with radiation damage (i.e., vacancies and recoil damage that form amorphous zones) on He diffusion in magnetite. The theoretical results show that He diffusion is purely isotropic, and that defect-free magnetite is more He diffusive than indicated by experimental data on natural specimen. Interestingly, the obtained theoretical trapping energy of vacancies and recoil damage are very similar to those obtained from experimental diffusion data. These results suggest that He diffusion in magnetite is strongly controlled by the presence of vacancies and radiation damage, even at very low damage dose. We propose that, when using magnetite (U-Th)/He thermochronometry, the impact of vacancies and radiation damage on He retention behavior should be integrated.

Keywords: magnetite; (U-Th)/He; geochronology; thermochronology; Density Functional Theory; He diffusion



Citation: Bassal, F.; Roques, J.; Corre, M.; Brunet, F.; Ketcham, R.; Schwartz, S.; Tassan-Got, L.; Gautheron, C. Role of Defects and Radiation Damage on He Diffusion in Magnetite: Implication for (U-Th)/He Thermochronology. *Minerals* **2022**, *12*, 590. <https://doi.org/10.3390/min12050590>

Academic Editor: Jim Lee

Received: 9 March 2022

Accepted: 2 May 2022

Published: 6 May 2022

Publisher's Note: MDPI stays neutral with regard to jurisdictional claims in published maps and institutional affiliations.



Copyright: © 2022 by the authors. Licensee MDPI, Basel, Switzerland. This article is an open access article distributed under the terms and conditions of the Creative Commons Attribution (CC BY) license (<https://creativecommons.org/licenses/by/4.0/>).

1. Introduction

Magnetite ($\text{Fe}^{2+}\text{Fe}^{3+}_2\text{O}_4$) crystallizes in a wide variety of geological environments through magmatic and hydrothermal processes, and can also be found as a detrital or authigenic mineral in sedimentary rocks [1,2]. It is a common accessory mineral in magmatic Ni–Cu–Platinum–Group Element (PGE) sulfide deposits from massive sulfide ores [3,4]. Hydrothermal magnetite is found in porphyry Cu–Mo–Au deposits [5,6]. Magnetite is also a primary constituent of iron oxide–apatite (IOA) deposits, or Kiruna-type, for which a magmatic versus hydrothermal origin is still debated (e.g., [7,8]). In addition to the interest in magnetite as a petrogenetic indicator for ore deposits [4,6,9,10], magnetite has also received a lot of attention as a product of serpentinization of the lithospheric mantle at slow-spreading ridges owing to its remarkable physical [11,12] and chemical properties [13–16].

Due to the petrological importance of magnetite, during the last fifteen years special attention has been devoted to the development and application of the magnetite (U-Th)/He thermo-geochronology method (e.g., [17–21]). Knowledge of helium diffusivity in magnetite is a prerequisite for the geological interpretation of magnetite (U-Th)/He data. The

first and only He diffusion dataset was obtained on a magnetite crystal from the Bala Cretaceous kimberlite [17] and revealed He retentive behavior, with a calculated closure temperature of $\sim 250^\circ\text{C}$ assuming $10^\circ\text{C}/\text{Myr}$ cooling and a sphere equivalent radius of $250\ \mu\text{m}$. The discovery of such a high closure temperature has paved the way for research into the use of the magnetite (U-Th)/He method to date the exhumation of mafic and ultramafic rocks [19,21], which are characterized by a scarcity of minerals that can be analyzed with (U-Th)/He thermochronometers. This new tool has been used to constrain the timing and duration of fossil hydrothermal mineralization and on serpentinite exhumation in a subduction-collision zone [20,22], respectively. In combination with ^3He production data, the magnetite (U-Th)/He method has been used to access the cosmic-ray exposure ages of detrital magnetite [23].

However, the He diffusion dataset obtained on the Bala magnetite also revealed a complex He diffusion pattern at low temperatures, with a few percent of the He released at a lower temperature than expected [17]. In order to understand this unexpected behavior and to better constrain the diffusion and thus the retention of He in magnetite, we have developed a theoretical approach to model He diffusion in magnetite. With this approach, we can probe the effect of crystal defects on He diffusivity, which may actually account for the low temperature He diffusion behavior observed by Blackburn et al. [17]. We used the multiscale theoretical approach developed in our team, which was successfully used in previous works [24–29]. The combined theoretical and experimental data demonstrate that the impact of crystal defects (e.g., Frenkel pairs) and alpha recoil damage must be considered when characterizing He diffusive behavior over geological time scales.

2. Materials and Methods

2.1. Theoretical Multiscale He Diffusion Modeling

The multiscale approach combines periodic Density Functional Theory (DFT) calculations at the atomic scale [30,31] and Kinetic Monte Carlo (KMC) simulations [26] at the macroscopic scale. DFT calculations were performed to characterize the interstitial and vacancy sites for He insertion into the magnetite crystal model. The minimum-energy pathway (MEP) of the He diffusion process between sites was characterized using the Nudged Elastic Band (NEB) method [32,33]. The migration energy between He sites was calculated, and KMC simulations were carried out to determine the He effective activation energy and diffusion coefficient.

2.1.1. Theoretical Computational Details

We first optimized a magnetite crystal cell starting from the chemical formula $[\text{Fe}^{3+}]^{\text{A}}[\text{Fe}^{3+}\text{Fe}^{2+}]^{\text{B}}\text{O}_4$ where A corresponds to tetrahedral sites occupied by the Fe^{3+} and B corresponds to octahedral sites occupied by an equal number of Fe^{2+} and Fe^{3+} ions [34]. Under geological conditions, Fe_3O_4 crystallizes in the spinel structure with a face-centered cubic (FCC) unit cell which is characterized by a lattice constant of $8.396\ \text{\AA}$ [35,36]. The cubic cell contains 32 O^{2-} anions, 16 Fe^{3+} cations and 8 Fe^{2+} cations. The FCC oxygen lattice defines 64 tetrahedral interstices and 32 octahedral ones. Fe^{3+} cations occupy 8 of the 64 tetrahedral sites, whereas the octahedral sites are occupied by 8 Fe^{2+} and 8 Fe^{3+} ions. Figure 1 shows the crystal structure of one cell used in this study, with tetrahedral and octahedral Fe sites.

In addition, as magnetite belongs to the class of ferrites, its ferrimagnetism properties were incorporated into the calculations. Magnetite lattice is composed of two magnetic ferromagnetic sub-lattices that are anti-ferromagnetically coupled together. The net magnetic moment of sub-lattice A is anti-parallel to the net magnetic moment of sub-lattice B. Spins of tetrahedral $[\text{Fe}^{3+}]^{\text{A}}$ and octahedral $[\text{Fe}^{3+}]^{\text{B}}$ cancel each other, and the ferrimagnetism properties of magnetite depend only on the octahedral $[\text{Fe}^{2+}]^{\text{B}}$. Unlike paramagnetic materials, ferrimagnetic substances such as magnetite are characterized by a net spin. To characterize the magnetic properties of magnetite, in particular for its iron atoms, we used spin-polarized DFT calculations. To be consistent with our previous studies [27–29], we chose the Perdew–Burke–Ernzerhof (PBE) functional exchange correlation potential.

Structural, electronic and magnetic proprieties of pure magnetite cubic unit cell are first investigated and compared to literature results.

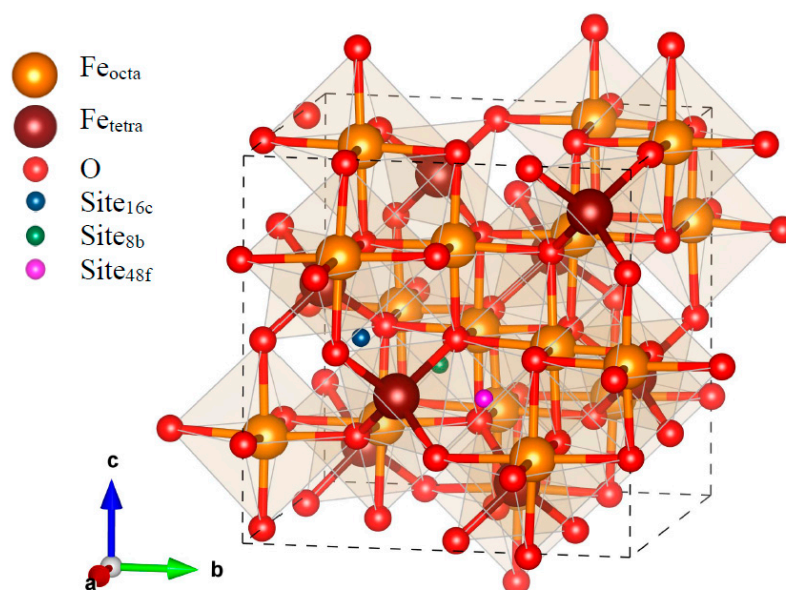


Figure 1. Magnetite unit-cell used in this study for DFT calculations, with the three possible He insertion sites (16c, 8b and 48f).

The cubic unit cell (Table 1 and Figure 1) has been considered as large enough to avoid a volume dilation of the system after He atom addition. Nevertheless, we performed numerous additional calculations with a super-cell characterized by a duplication along the a -axis ($2\vec{v}_1 \times \vec{v}_2 \times \vec{v}_3$) to (i) confirm the calculation results obtained with the cubic unit-cell and thus confirm the potential of our model, and (ii) better investigate the He jump between adjacent sites with the Nudged Elastic Band (NEB) method.

Table 1. Structural properties of magnetite ($\vec{v}_1 \times \vec{v}_2 \times \vec{v}_3$) and ($2\vec{v}_1 \times \vec{v}_2 \times \vec{v}_3$) cubic-cell and He insertion energies for interstitial sites, from PBE+U Density Functional Theory simulations.

Defect-Free Crystal	a (Å)	b (Å)	c (Å)	$E_{\text{insertion}}$ (eV)		
				16c	8b	48f
Cubic cell ($\vec{v}_1 \times \vec{v}_2 \times \vec{v}_3$)	8.49	8.49	8.49	1.13	3.96	unstable
Cubic cell ($2\vec{v}_1 \times \vec{v}_2 \times \vec{v}_3$)	16.98	8.49	8.49	1.10	-	-

2.1.2. Atomic Scale

Periodic DFT [30,31] was used to perform geometrical optimizations and energy calculations over many configurations with different atom locations. Plane wave basis sets were used to solve the Kohn–Sham equations and to calculate the self-consistent total energy. The generalized gradient approximation (GGA) and, in particular, the Perdew–Burke–Ernzerhof (PBE) [37] functional exchange correlation potential, was used within the framework of the projector augmented wave method (PAW) [38,39]. For each atom, ionic cores were described with PAW pseudo-potentials, and valence electron configurations were defined as $3d^7 4s^1$ for Fe; $2s^2 2p^4$ for O. The magnetite structure used in this study was taken from the magnetite crystallographic information file by [35]. Simulations were carried out with the Vienna Ab-initio Simulation Package (VASP) [40,41].

Systems containing transition elements like iron are characterized by strong electronic correlations, in particular for the 3d correlated electrons [42–45]. Thus, according to our previous computational works [27–29], the addition of a corrected parameter (DFT+U [27–29]),

the so-called Hubbard parameter, was necessary for the Fe atom to improve the description of the electronic and magnetic properties of magnetite. The Dudarev approach [46] was chosen to correctly describe iron valence electrons, in particular, the 3d strong intra-atomic electronic correlations with the DFT method by adding an on-site Coulomb repulsion U and an on-site exchange interaction J to the DFT Hamiltonian. In this case, the Hubbard effective parameter U_{eff} is defined as $U_{\text{eff}} = U - J$. The value of $U_{\text{eff}} = 3.75$ eV ($U = 4.75$ eV and $J = 1.0$ eV) was optimized according to an analytical strategy that consisted of testing different U_{eff} values between 2 and 7 eV, that are in the range of literature values [47,48]. Results were compared to experimental data, such as experimental magnetic moments, structural parameters and density of states of magnetite lattice. We chose the U_{eff} value which gave the best agreement between computational and experimental results. This U_{eff} value is in good agreement with literature theoretical investigations, which provide values between 3.5 eV and 4 eV [48]. Calculation parameters were selected as described in our previous works [24–29]. A cutoff energy of 450 eV was used for the plane-wave expansion of the wave function to converge the relevant quantities. The integration over the Brillouin zone was performed using the Monkhorst–Pack scheme [49] with a mesh of $3 \times 3 \times 3$ k-points for the $(\vec{v}_1 \times \vec{v}_2 \times \vec{v}_3)$ cubic unit-cell and $2 \times 1 \times 1$ for the $(2\vec{v}_1 \times \vec{v}_2 \times \vec{v}_3)$ supercell.

However, since natural crystals contain crystal defects, such as point defects (i.e., vacancies) or damage associated with the radioactive decay of U and Th, we also studied the impact of these types of defects on the He behavior. The impact of point defects on He diffusion was analyzed by removing one tetrahedral Fe^{3+} from the supercell $(2\vec{v}_1 \times \vec{v}_2 \times \vec{v}_3)$. Once all possible interstitial sites were identified for the considered cubic unit cell for a defect-free magnetite structure (Figure 2) and for the magnetic structure containing a defect (Figure 3), simulations based on the NEB method [33] were carried out to determine migration energy (E_{mig}^{ij}) for each possible jump between 16c sites, points defects and recoil damage (Table 2, Figures 2 and 3).

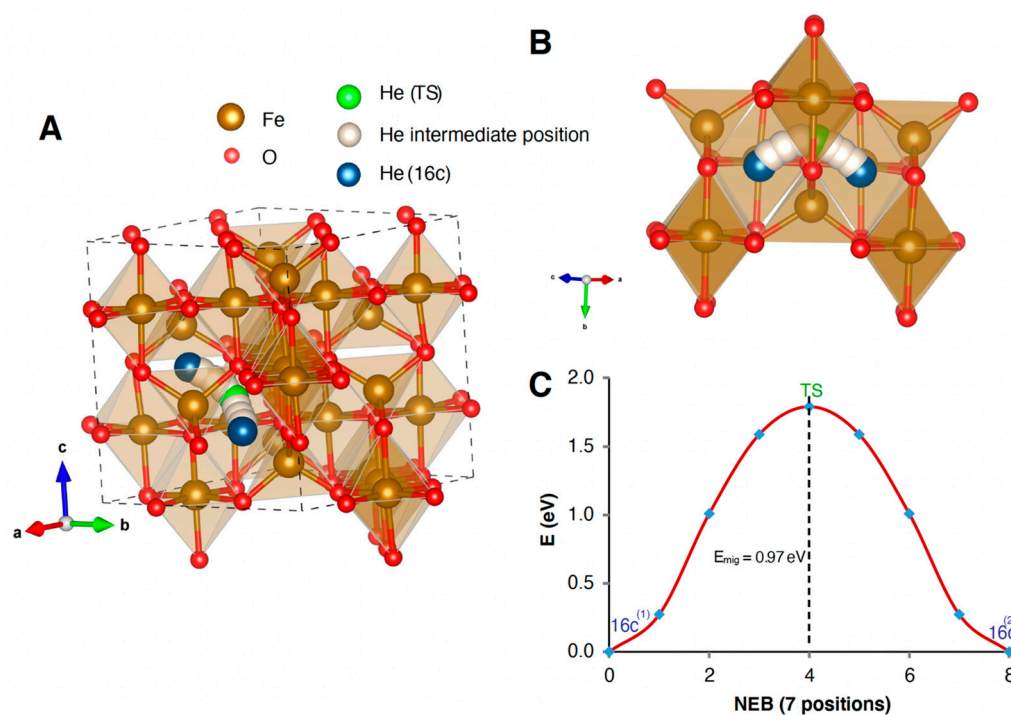


Figure 2. Migration energy pathway between two 16c interstitial sites. (A,B) view the NEB migration pathway along two different perspectives. (C) Evolution of the He energy between the interstitial sites 16c passing through the Transition State point (TS).

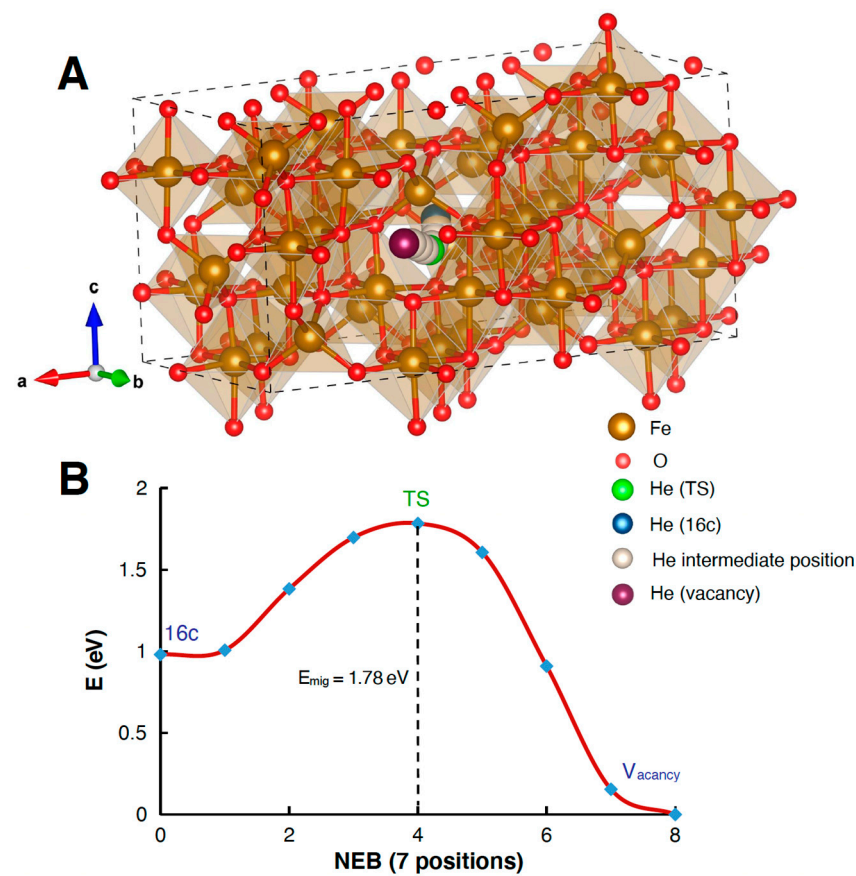


Figure 3. Crystallographic Fe^{3+} point defect in the $(2\vec{v}_1 \times \vec{v}_2 \times \vec{v}_3)$ cell. **(A)** view of the NEB migration pathway. **(B)** Evolution of the He energy between the interstitial site 16c and the vacancy site, passing through the transition state (TS).

Table 2. Theoretical He diffusion data for magnetite.

	$E_{\text{insertion}}$ (eV)	E_{mig} (eV)	E_a (eV)	D_0 (cm^2/s)	T_c ($^{\circ}\text{C}$) * $R_s = 250 \mu\text{m}$	T_c ($^{\circ}\text{C}$) * $R_s = 500 \mu\text{m}$
Theoretical study						
Defect-free crystal $(\vec{v}_1 \times \vec{v}_2 \times \vec{v}_3)$	1.13	0.97	0.97	3.07×10^{-3}	35	47
Defect-free crystal $(2\vec{v}_1 \times \vec{v}_2 \times \vec{v}_3)$	1.10	0.99	0.99	3.07×10^{-3}	-	-
Crystallographic Fe^{3+} point defect **	0.50	1.78	-	-	-	-
Recoil damage	0	2.1 to 2.28	-	-	-	-
Experimental study						
Cubic cell $(2\vec{v}_1 \times \vec{v}_2 \times \vec{v}_3)$	16.98	8.49	8.49		250	262

* The closure temperature (T_c) is computed for two crystal sizes and a cooling rate of $10^{\circ}\text{C}/\text{Myr}$. ** in the $(2 \times \vec{v}_2 \times \vec{v}_3)$ cell.

2.1.3. Macroscopic Scale

Finally, DFT results were used as the basis for Kinetic Monte Carlo (KMC) simulations to simulate the effective activation energy and pre-exponential factor for He diffusion in magnetite. The KMC method [50] simulates the time-dependent trajectories of the He

atom diffusion in the free space using transition rates that depend on the migration energy barriers, E_{mig}^{ij} , to jump from initial to final states. According to Transition State Theory (TST) [50,51], the thermal jumping process of an He atom can be described using the probability of jumps (Γ^{ij}). Γ^{ij} is characterized by an attempt frequency (ν_0) and depends exponentially on the temperature (T). The attempt frequency, ν_0 , can be defined using the Vineyard approximation [50], based on the harmonic frequencies of the He atom at the initial ground and transition states (see [27] for more details).

Afterward, the jump probabilities for all possible transitions $S_0 \rightarrow S_{1,2,3} \dots n$ between an initial site S_0 and all neighboring sites $S_{1,2,3} \dots n$ can be calculated. For each initial site, S_0 , the total jump probability, Γ^{Tot} , can be obtained as the sum of the jump probabilities to all neighbor sites. The residence time is calculated as the inverse of the total jump probability, corresponding to the time required for passing from the initial site to a neighboring one. Considering all the residence times for all the sites, the mean square displacement (MSD) of the He diffusion can be calculated. Thus, the diffusion coefficient, D_T , at temperature T for a He atom can be calculated based on Einstein's diffusion equation relating the spread of random trajectories to their duration [51]. More methodological details can be found in our previous works [24–29].

2.2. Theoretical Damage Quantification

Different types of defects can be present in the magnetite lattice, such as vacancies (Frenkel-pair defects) and recoil damage. They are produced mostly from U and Th alpha decay as Sm content is low in magnetite, but vacancies can also be present during magnetite crystallization. During alpha decay, atoms will be displaced during each decay event, and point-defect and recoil damage will be produced by the alpha particle and the recoil of the daughter element [52], respectively. We can quantify the amount of defects produced in magnetite associated with alpha decay using the SRIM “The Stopping and Range of Ions in Matter” software [53]. For the ^{238}U decay chain (mean energy of 5.36 MeV), 230 point-defects and 1600 displacements from recoil damage are produced per alpha decay. For the damage from each recoil, the vacancy density is 7 per angstrom, leading to a large damage zone, whereas the maximum density of each point defect caused by the alpha particle is 0.02 per angstrom, near the end of the alpha particle stopping range, where it reaches its maximum, low enough to keep point defects without extended crystal reconfiguration. When calculating damage fraction due to a given dose, in the following we assume that due to the high density of vacancies produced by recoil the lattice partially relaxes, creating amorphous domains in which He can be stored without energy cost (zero insertion energy) because they contain zones where atoms are far from each other, similar to cavities. The density of such domains is lower than the initial density of vacancies, by a factor g that can be estimated. For example, if a cluster of 10 point-defects is created along the recoil track, they collapse into a single amorphous domain, resulting in a g of 0.1. We leave it as a free parameter which gets a maximal theoretical value of 1. On the other hand, the vacancies created along the alpha particle survive due to their low density and they remain as point defects. We assume that most point defects are created along the alpha track, whereas the recoil produces recoil damage, as amorphous domains, having a density lower than the initial vacancy density by a factor g .

An important issue is the possible annealing of the defects. This annealing occurs in part immediately as a self-annealing due to the irradiation itself. It could apply to the point-defects which can be repaired by moving a single atom, but it is probably inefficient for recoil damage where the lattice has been eradicated. For lack of knowledge, we assume that there is no such annealing. Another possible process is thermal annealing acting over geological times and during the degassing experiments. In the former case we presume that the temperature needed to get a significant annealing is high (above 200 °C) and this is compatible with the age for the sample Rocher Blanc magnetite from the Schistes Lustrés (Western Alps) [21] (see below). During the degassing experiments, the annealing is usually negligible, although the temperature is high, due to the short dwelling time of the steps.

3. Results

The aim of simulations is to provide the distance and the hopping rate between sites, which are the main ingredients for the computation of the diffusion coefficient. The rates are not obtained from a dynamical simulation, but they derive instead from a statistical calculation of the thermal motion carried out by the TST. This latter calculation uses as input the energy landscape probed by the diffusing atom, in particular, the migration energies. The key role of the DFT is to provide this energy information, taking into account the quantum effects of electrons. The main limitation of this approach is that it relies on a static representation of the system, ignoring correlations in the thermal motion of atoms, like phonons which could be followed in a molecular dynamic simulation, but which would omit some quantum effects. Obviously, the rates depend on the energy depth of the sites, and this leads to an investigation of the different types of sites, particularly those created by crystal defects.

3.1. Defect-Free Magnetite Structure

Three insertion sites named 16c, 8b & 48f were identified in the magnetite cell ($\vec{v}_1 \times \vec{v}_2 \times \vec{v}_3$) as displayed in Figure 1. The insertion energies range from 1.13 to 3.96 eV for the 16c and 8b sites, respectively, and cannot be calculated for the 48f site as it is unstable (Table 1). One can note that the insertion energy for the 8b site is more than three times higher than for the 16c site, making it unsuitable to host an He atom as the needed energy to occupy it is too high. There are four 16c sites in a cell of 56 atoms leading to 1.3×10^{21} sites/g. In addition, we repeated the same calculations (for the 16c site) by duplicating the cell ($2 \times$ the cubic cell along the a-axis) to confirm the consistency of our cell model. No significant differences were found, as only a minor difference of 0.03 eV was obtained for the insertion energy (Table 1). The computed NEB migration energy between the 16c sites is 0.97 eV for a cubic cell or 0.99 eV in the case of a doubled cell (Table 2).

The energy path between 16c sites is presented in Figure 2, and each 16c site is surrounded by 12 identical ones, allowing as many possible jumps. The average coordinate variance of a jump is $7/24$ times the square of the cell size (21.0 \AA^2) and it is identical for the three coordinates, so that the diffusion is purely isotropic. Finally, the KMC simulation using the approach described in [26] allows us to calculate a 3D activation energy E_a of 0.97 eV and a pre-exponential D_0 factor of $3.07 \times 10^{-3} \text{ cm}^2/\text{s}$ for He diffusion in a perfect magnetite lattice. Since He is found to only diffuse between 16c sites in the case of the perfect lattice, the activation energy is equal to the migration energy between those sites. The closure temperature (T_c) is $35 \text{ }^\circ\text{C}$ for a crystal size of $250 \text{ }\mu\text{m}$ and a cooling rate of $10^\circ\text{C}/\text{Ma}$ (Table 2) based on the equation of [54]. This result is different from measurements of natural magnetite, for which a T_c of $250 \text{ }^\circ\text{C}$ was obtained for the same radius and cooling rate ([17]; Table 2). Helium diffusion results obtained for a defect-free magnetite structure is reported in the Arrhenius diagram on Figure 4A, where experimental diffusion results from Blackburn et al. [17]; are plotted for comparison.

3.2. Magnetite Structure Containing Crystallographic Defect or Radiation Damage

When an atom is knocked out of place by an alpha particle or recoil nucleus, a vacancy is left, but the ejected atom can create an obstruction when deposited in a diffusion path. However, as the diffusion is isotropic, this obstruction effect can be neglected because the obstructing atom can be easily bypassed in 3D. Therefore, we will discard the obstruction mechanism and we will consider only the trapping effect of vacancies. To estimate the impact of a crystal defect such as a point defect on He diffusion, one Fe^{3+} tetrahedral atom was removed from the supercell ($2\vec{v}_1 \times \vec{v}_2 \times \vec{v}_3$). The removal of one tetrahedral Fe-atom creates a vacancy which is characterized by an He insertion energy, E_{ins} , of 0.50 eV and a migration energy of 1.78 eV (Table 2 and Figure 3) to jump from the vacancy to the 16c interstitial site. Although other iron atoms, or oxygen atoms, can be knocked out, we assume that these energies are still representative. The evolution of \widetilde{D}_0 as a function of the point-defect content has been modeled using Equation 1 from Gerin et al. [24], with

no annealing. The frequency factor \widetilde{D}_0 of a crystal with defects becomes $\widetilde{D}_0 = D_0/f$, with the defect fraction f ranging from 0 to 1. Using SRIM modeling, we estimated the amount of point defects associated with the alpha-decay for the Bala kimberlite magnetite used in the diffusion study of [17,18]. We calculate 1.82×10^{22} atoms per gram of magnetite. Using the magnetite (U-Th)/He age of 94 Ma, a mean U content of 0.2 ppm and a mean Th/U ratio of 0.2 [18], we modeled an alpha dose of 6.5×10^{13} alpha/g and a number of point-defects created by the α -particles of 1.5×10^{16} d/g, leading to a density (normalized to the number of sites) $f_{\text{point-defect}} = 1.1 \times 10^{-5}$. The associated \widetilde{D}_0 is $2.7 \times 10^2 \text{ cm}^2/\text{s}$. For those values, a T_c of 144°C is obtained for a crystal size of $250 \mu\text{m}$ and a cooling rate of $10^\circ\text{C}/\text{Ma}$. This result is also reported in the Arrhenius diagram of Figure 4A. The diagram exhibits a pattern typical of multi-domain diffusion, with the small domain's contribution dominating at low temperature. Therefore, we will restrict the comparison to our calculation to the high temperature region, on the left side, where the data converge to a stable slope representative of the large domain. We see that the slope (activation energy) is a better match for the high temperature experimental data, but the calculated points are still much higher than the data.

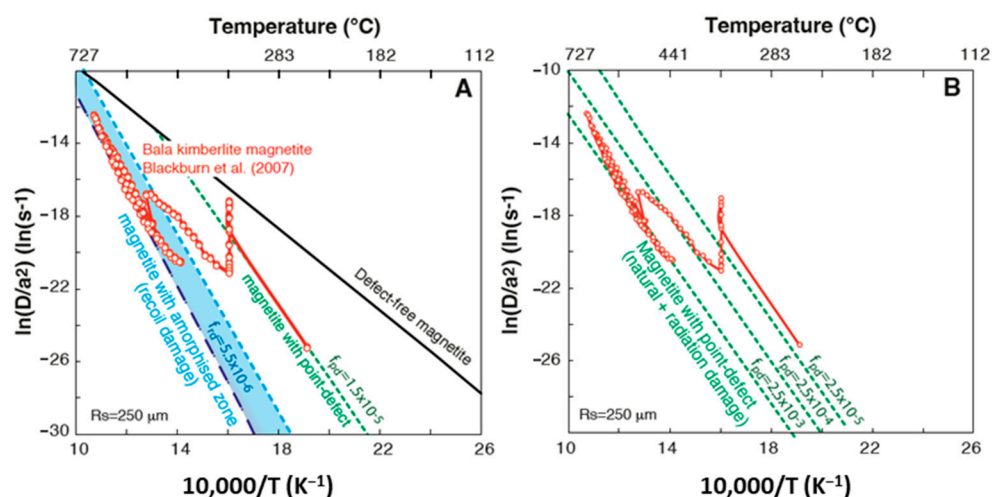


Figure 4. Arrhenius diagram ($\ln(D/a^2)$ vs. $10,000/T$) comparing He diffusion data obtained experimentally on a Bala Kimberlite magnetite grain [17] with the results of our calculations. (A) He diffusion properties obtained using DFT calculations, for a sphere equivalent radius of $250 \mu\text{m}$, for defect-free magnetite (black line), and magnetite with point defect (green dashed line) and recoil damage ($E_a = 2.1 \text{ eV}$ (light blue dashed lines) and 2.28 eV (dark blue dashed lines), with a g factor of 0.023) concentrations estimated for Bala magnetite, \widetilde{D}_0 using activation energies from Table 1 and frequency factors of 3.07×10^{-3} , 2.7×10^2 , and $1.8 \times 10^3 \text{ cm}^2/\text{s}$, respectively. (B) He diffusion properties obtained using DFT calculations, for a sphere equivalent radius of $250 \mu\text{m}$, with different point defect fractions of 2.5×10^{-5} , 2.5×10^{-4} and 2.5×10^{-3} , that will be associated with the combination of radiation damage induced point defects and point defects formed during magnetite crystallization (named here natural point defects).

When comparing to experimental data, it is clear that not only are point defects involved, but recoil damage is also. In the case of recoil damage associated with alpha decay, we can assume as a first approximation that a free space will be created that is large enough to accommodate a He atom without any energy constraint or cost. That corresponds to an He insertion energy of 0 eV in the recoil damage cavity, compared to 1.13 eV for a pristine lattice or 0.50 eV for a point defect. Thus, the energy barrier (E_{mig}), in this case, will range from 2.10 eV ($1.13 + 0.97 \text{ eV}$) to 2.28 eV ($0.50 + 1.78 \text{ eV}$). This approach has already been applied to apatite and zircon and allows prediction of the maximum migration energy [24,25,55]. As for the point-defect case, a recoil damage amount ($f_{\text{recoil-damage}}$) is calculated for the Bala kimberlite magnetite which reaches 7.6×10^{-5} , if

we adopt the limiting value $g = 1$, with an associated \widetilde{D}_0 of $40 \text{ cm}^2/\text{s}$. In that case, a T_c of $254\text{--}298 \text{ }^\circ\text{C}$ is obtained for a crystal size of $250 \text{ }\mu\text{m}$ and a cooling rate of $10 \text{ }^\circ\text{C}/\text{Ma}$. The activation energy (E_a) is almost identical to that of the high temperature data of natural magnetite [17]. However, the line is shifted downward, which is not surprising since we adopted a g parameter equal to its maximal theoretical value of 1. This value is unrealistic because we expect that if amorphization takes place, many point-defects will merge into a single amorphous domain. The amorphous zone would at least be on the order of the cell size, and we calculated the g value to be 0.023. We provide a complete and full description of the calculation in the supplementary section. In brief, the recoiling daughter produces 1600 point-defects over a range of $200\text{--}300 \text{ }\text{\AA}$ with a maximal linear density of $7 \text{ d}/\text{\AA}$, meaning that along the track, the distance between defects is smaller than the inter-atomic distance. In such conditions, the crystal will locally collapse, producing an amorphous domain, then assuming that from the 1600 point-defects we are left with a single amorphous domain. The volume of the domain can be inferred approximatively from the number of displaced atoms. A crystal cell is a cube of length $8.5 \text{ }\text{\AA}$ containing 56 atoms, so that 1600 displacements involve $1600/56 = 28.6$ cells which collapse into disorder. The domain shape is likely an elongated cylinder, but for the sake of convenience and taking into account all the orientations, we represent it as a cube of size $28.6^{1/3} = 3.06$ units of cell size. As each cell intercepts four lines of a given direction (four sites per cell) the number of lines intercepted by the amorphous zone is $3.06^2 \times 4 = 37$. Therefore, we get $n = 37$ in Equation (12) of the supplementary section. As a conclusion from an initial point-defect number of 1600, we get an equivalent number of defects of 37, that when combined with the meaning that a factor $g = 37/1600 = 0.023$ that should be applied to the initial point defect density to get the equivalent density of the amorphization. Such a value would shift the $f_{\text{recoil-damage}}$ up to 1.8×10^{-6} leading to a \widetilde{D}_0 value of $1748 \text{ cm}^2/\text{s}$ and a T_c of $215\text{--}257 \text{ }^\circ\text{C}$, the considering is reported in Figure 4A.

4. Discussion

4.1. He Diffusion in Magnetite Structure

4.1.1. Theoretical Investigation of He Diffusion

The DFT theoretical approach reveals that He diffusion in magnetite is purely isotropic due to the cubic symmetry of the lattice, with a high He diffusion rate as illustrated by the computed closure temperature of $35 \text{ }^\circ\text{C}$ for a sphere radius of $250 \text{ }\mu\text{m}$. The computation indicates that helium diffusion in defect-free magnetite is much faster than in natural magnetite. The computed closure temperature for defect-free magnetite is $200 \text{ }^\circ\text{C}$ below that reported in the literature for natural magnetite [17,19,21].

The DFT approach shows however that if crystal defects and/or radiation damage are present in the magnetite lattice, He diffusion is significantly slowed down, and the retentive He behavior observed for natural magnetite can be reproduced by adjusting the amount of these defects in the magnetite lattice, as already demonstrated for zircon [25]. This would imply that He atoms are mostly trapped in defects and radiation damage which therefore control the diffusion kinetics. Since the migration energy of He from those defects and damage are different, as shown in Table 2, helium atoms are either located in an insertion site, a point defect or a recoil damage zone will require a different thermal energy to diffuse out of the grain. In other words, in the case of natural magnetite, both degassing behavior and inferred closure temperature will depend on the respective amount of these defects.

4.1.2. Defect and Damage Impact on He Diffusion

As already quantified using the DFT approach for other minerals such as apatite and zircon [24,25], defects and, more specifically, radiation damage act as traps [56,57] and strongly influence He retention in the crystal structure. It is interesting to note that the He diffusion data of Blackburn et al. [17] can be very well reproduced, as shown in Figure 4A, using the He diffusion damage model of Gerin et al. [24] and the irradiation dose calculated using a sphere equivalent radius (R_s), the U, Th content and crystallization age of the

Bala magnetite [18]. The conversion of the irradiation dose into amorphous zone volume indicates that this zone would be at least in the order of the cell size, and for this reason we used a g value of 0.02. More specifically, the experimental high temperature diffusion dataset of Blackburn et al. [17] ($T > 440$ °C), from which the authors calculated T_c , are well reproduced and similar activation energy and frequency factor are found (Figure 4A and Table 2). In addition, the activation energy of crystallographic defects is similar to that obtained from the lower temperature part of the Bala magnetite dataset ($T < 440$ °C). The experimental dataset can be partially reproduced using the crystallographic defect fraction produced during atomic displacements associated with radiation damage (Figure 4 and Table 2). However, a higher atomic fraction of defects, in the 2.5×10^{-3} to 1.5×10^{-5} range (or 0.25 to 0.0015 %) allows us to reproduce the experimental data, as illustrated in Figure 4B. Having a higher crystallographic defect dose in a natural crystal is not surprising, as the calculated defect fraction only represented the defects produced during alpha decay. In natural magnetite, crystallographic defects associated with crystal growth and chemical substitutions are naturally present and will then increase the defect fraction. This value is difficult to quantify and will be variable for each magnetite crystal. However, the iron tetrahedral and octahedral sites' occupations and vacancies formation have been already investigated. At low temperatures, magnetite crystallizes with the inverse spinel structure with half of the Fe^{3+} in the tetrahedral site (A) and with Fe^{2+} and half of the Fe^{3+} in the octahedral sites. This trivalent divalent distribution evolves progressively with increasing temperature towards the normal spinel structure, i.e., with all Fe^{2+} in tetrahedral sites and Fe^{3+} in octahedral sites. Simulation of magnetite site occupancy by Hallström et al. [58] using the thermochemical dataset by Sundman [59] shows that between 400 and 600 °C, divalent Fe occupies between 5 and 10% of the tetrahedral sites. In addition to this temperature dependency of site occupancy, which leads to a deviation from the normal spinel end-member structure, magnetite can also exhibit non-stoichiometry.

In addition, depending on oxygen fugacity and temperature, the iron/oxygen ratio can depart from $\frac{3}{4}$ and magnetite becomes $\text{Fe}_{(3-d)}\text{O}_4$, with d being positive at high $f\text{O}_2$ and negative towards low $f\text{O}_2$ [60]. Under high $f\text{O}_2$ conditions, iron deficiency is accounted for by formation of octahedral vacancies, whereas under reducing conditions, excess Fe^{2+} enters vacant octahedral sites [59]. Under the $f\text{O}_2$ of natural magnetite formation (e.g., below the magnetite/hematite buffer), and based on the dataset of Sandman [59], interstitial Fe^{2+} is actually more likely than octahedral vacancies. Another alternative to produce octahedral vacancies is the formation of iron Frenkel pairs corresponding to the formation of an octahedral vacancy along with an interstitial iron atom, the stability of which in the stoichiometric magnetite structure has been investigated by Arras et al. [61] using the DFT + U method. The number of iron Frenkel pairs in stoichiometric magnetite ($d = 0$) has been evaluated to 10^{-5} per lattice molecule at 800–900 °C [60]. Additionally, octahedral iron vacancies can be created when minor (i.e., silicon, [62]) and trace (i.e., uranium, [63]) elements are incorporated into the magnetite structure. As a result, the number of defects in a crystal will exceed those formed during alpha decay, depending on the crystallization temperature, impurity content, and $f\text{O}_2$.

4.2. Implication for Magnetite (U-Th)/He Thermo-Geo-Chronometer

Computed He diffusion simulations using the DFT approach show that He retention in natural magnetite is controlled, in the first place, by the concentration of radiation damage and, in the second place, by the concentration of point defects. Based on the obtained activation energy of 2.1 and 2.28 eV and frequency factor in this study, we modeled the evolution of the closure temperature in magnetite as a function of the defect/damage fraction. The results are reported in Figure 5, in addition to the closure temperature obtained on the Bala kimberlite magnetite [17] and expected for the Rocher Blanc magnetite, that comes from a mid-Tertiary exhumed high-pressure ophiolite from the Western Alps (France) [21] using the age, U and Th content and equivalent radius of those samples. The DFT modeling accounts for the increase in the closure temperature with the damage

dose, and confirms the previous closure temperatures proposed for natural magnetite [17]. The results for natural magnetite samples [17,21] are in addition better explained with the activation energy of 2.28 eV in comparison with the value of 2.1 eV (Table 2), using the calculated frequency factor for amorphous zone production with a g factor of 0.02. This confirms that large defect zones are created during alpha decay with amorphous cores where He atoms are trapped.

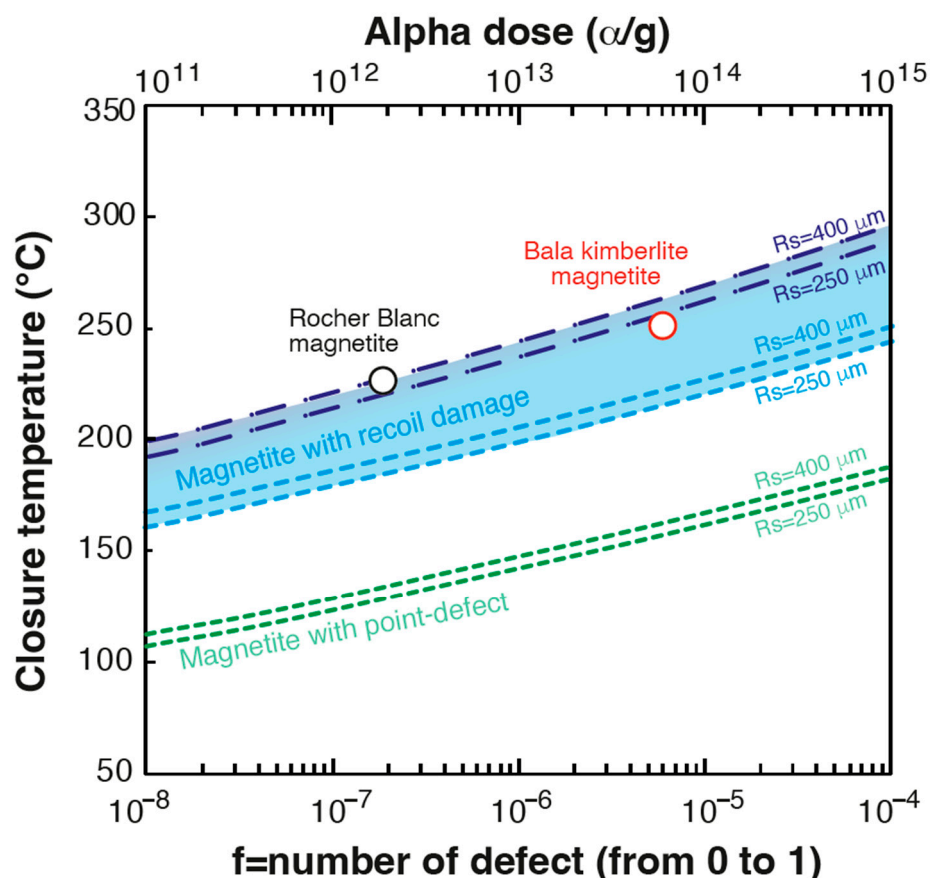


Figure 5. Evolution of closure temperature (T_c) as a function of defect fraction (from 10^{-8} to 10^{-4}) and alpha dose (10^{11} to 10^{15} alpha/g), for a magnetite with point defects and with recoil damage ($E_a = 2.1$ eV (light blue dashed lines) and 2.28 eV (dark blue dashed lines), with a g factor of 0.023). Calculations have been done for magnetite crystals of 250 and 400 μm size radius. Data for Bala kimberlite magnetite [17] and Rocher Blanc ophiolite magnetite [21] are reported.

These results have important implications for the interpretation of magnetite (U-Th)/He thermo-geo-chronological data. First, they show that He is very well retained in magnetite, even in young crystals with low damage dose, with $T_c > 150^\circ\text{C}$, and that the (U-Th)/He method applied to magnetite (MgHe) can be used as a geochronometer for magnetite which crystallizes at low temperature ($<150^\circ\text{C}$). Second, the results demonstrate that He retention evolves with the damage dose, and the MgHe method can be used as a thermochronometer, with a typical T_c of $220\text{--}280^\circ\text{C}$, as already demonstrated by Cooperdock et al. [19] and Schwartz et al. [21], who inverted MgHe data to infer a thermal history. However, consideration of the damage dose is essential to properly interpret MgHe ages and quantify the thermal history. Interestingly, based on studies conducted to date, the U and Th content of natural magnetite is relatively constant (e.g., [17,21]), in the order of a dozen ppb, and we can deduce that He retention and, consequently, T_c will be similar for each geological case. Low dispersion in MgHe ages, i.e., within the analytical dispersion,

should be expected for magnetite with similar diffusion domains, as the He retention behavior in magnetite should be similar for grains with the same geological history.

5. Conclusions

This study has explored He diffusion in magnetite for the purpose of understanding the (U-Th)/He thermochronometer and geochronometer. Employing a multi-scale theoretical approach, we compute the impact of two different types of defects (i.e., point defects and recoil damage) on He diffusion. We find that He diffusion in magnetite is purely isotropic and that He is retained in defect-free magnetite, but not at the same level inferred from experimental study. However, the obtained theoretical trapping energy of vacancies and recoil damage are very similar to those obtained from experimental diffusion data, showing that defect and damage strongly traps He atoms and alters He diffusion in magnetite. Using a damage model, we can predict the amount of displaced atoms during radioactive U-Th alpha decay and the point-defect and recoil damage dose. Using such a model, experimental diffusion data from the literature are well reproduced. We show that point defects and recoil damage control He retention in magnetite, even at very low damage dose. Closure temperature can vary by more than 50 °C, with T_c ranging from 200 to 280 °C, depending on the damage dose and crystal size. From these results, and typical U and Th contents encountered in magnetite, one can anticipate low MgHe age dispersion for most geological cases. The consideration of the damage dose is required to properly interpret MgHe ages and derive meaningful thermal histories.

Supplementary Materials: The following supporting information can be downloaded at: <https://www.mdpi.com/article/10.3390/min12050590/s1>, Text: Diffusion coefficient in presence of defects and amorphous zones.

Author Contributions: Conceptualization, F.B. (Fadel Bassal), J.R. and C.G.; methodology, F.B. (Fabrice Brunet) and J.R.; resources, J.R.; writing—original draft preparation, F.B. (Fadel Bassal) and J.R.; writing—review and editing, F.B. (Fadel Bassal), J.R., M.C., F.B. (Fabrice Brunet), S.S., R.K., L.T.-G. and C.G.; visualization, F.B. (Fadel Bassal) and C.G.; funding acquisition, C.G. All authors have read and agreed to the published version of the manuscript.

Funding: This research and F. Bassal salary has been funded by the Agence National de la Recherche—grant no. ANR-17-CE01-0012—RECA: Relation entre le Changement climatique et formation des latérites.

Acknowledgments: We would like to thank Christophe Diarra for his precious help in managing the IPNO cluster (GRIF).

Conflicts of Interest: The authors declare no conflict of interest. The funders had no role in the design of the study, in the collection, analyses, or interpretation of data, in the writing of the manuscript, or in the decision to publish the results.

References

1. Miller, D.N.; Folk, R.L. Occurrence of detrital magnetite and ilmenite in red sediments: New approach to significance of redbeds: Geological notes. *AAPG Bull.* **1995**, *39*, 338–345.
2. Phillips, S.C.; Johnson, J.E.; Clyde, W.C.; Setera, J.; Maxbauer, D.P.; Severmann, S.; Riedinger, N. Rock magnetic and geochemical evidence for authigenic magnetite formation via iron reduction in coal-bearing sediments offshore Shimokita Peninsula, Japan (IODP Site C0020): Authigenic magnetite offshore Shimokita. *Geochim. Geophys. Geosystems* **2017**, *18*, 2076–2098. [\[CrossRef\]](#)
3. Boutroy, E.; Dare, S.A.; Beaudoin, G.; Barnes, S.-J.; Lightfoot, P.C. Magnetite composition in Ni-Cu-PGE deposits worldwide: Application to mineral exploration. *J. Geochem. Explor.* **2014**, *145*, 64–81. [\[CrossRef\]](#)
4. Ward, L.A.; Holwell, D.A.; Barry, T.L.; Blanks, D.E.; Graham, S.D. The use of magnetite as a geochemical indicator in the exploration for magmatic Ni-Cu-PGE sulfide deposits: A case study from Munali, Zambia. *J. Geochem. Explor.* **2018**, *188*, 172–184. [\[CrossRef\]](#)
5. Canil, D.; Grondahl, C.; Lacourse, T.; Pisiak, L.K. Trace elements in magnetite from porphyry Cu–Mo–Au deposits in British Columbia, Canada. *Ore Geol. Rev.* **2016**, *72*, 1116–1128. [\[CrossRef\]](#)
6. Nadoll, P.; Angerer, T.; Mauk, J.; French, D.; Walshe, J. The chemistry of hydrothermal magnetite: A review. *Ore Geol. Rev.* **2014**, *61*, 1–32. [\[CrossRef\]](#)

7. Knipping, J.L.; Bilenker, L.D.; Simon, A.; Reich, M.; Barra, F.; Deditius, A.; Wälle, M.; Heinrich, C.; Holtz, F.; Munizaga, R. Trace elements in magnetite from massive iron oxide-apatite deposits indicate a combined formation by igneous and magmatic-hydrothermal processes. *Geochim. Cosmoch. Acta* **2015**, *171*, 15–38. [\[CrossRef\]](#)
8. Nyström, J.O.; Billström, K.; Henríquez, F.; Fallick, A.E.; Naslund, H.R. Oxygen isotope composition of magnetite in iron ores of the Kiruna type in Chile and Sweden. *GFF* **2008**, *130*, 177–188. [\[CrossRef\]](#)
9. Dare, S.A.S.; Barnes, S.-J.; Beaudoin, G.; Méric, J.; Boutroy, E.; Potvin-Doucet, C. Trace elements in magnetite as petrogenetic indicators. *Miner. Depos.* **2014**, *49*, 785–796. [\[CrossRef\]](#)
10. Huang, X.-W.; Sappin, A.-A.; Boutroy, E.; Beaudoin, G.; Makvandi, S. Trace Element Composition of Igneous and Hydrothermal Magnetite from Porphyry Deposits: Relationship to Deposit Subtypes and Magmatic Affinity. *Econ. Geol.* **2019**, *114*, 917–952. [\[CrossRef\]](#)
11. Maffione, M.; Morris, A.; Plümper, O.; Van Hinsbergen, D.J.J. Magnetic properties of variably serpentinized peridotites and their implication for the evolution of oceanic core complexes. *Geochem. Geophys. Geosystems* **2014**, *15*, 923–944. [\[CrossRef\]](#)
12. Oufi, O. Magnetic properties of variably serpentinized abyssal peridotites. *J. Geophys. Res.* **2002**, *107*, 2095. [\[CrossRef\]](#)
13. Brunet, F. Hydrothermal Production of H₂ and Magnetite From Steel Slags: A Geo-Inspired Approach Based on Olivine Serpentinization. *Front. Earth Sci.* **2019**, *7*, 17. [\[CrossRef\]](#)
14. Klein, F.; Bach, W.; McCollom, T.M. Compositional controls on hydrogen generation during serpentinization of ultramafic rocks. *Lithos* **2013**, *178*, 55–69. [\[CrossRef\]](#)
15. Klein, F.; Bach, W.; Humphris, S.E.; Kahl, W.-A.; Jöns, N.; Moskowitz, B.; Berquó, T.S. Magnetite in seafloor serpentinite—Some like it hot. *Geology* **2014**, *42*, 135–138. [\[CrossRef\]](#)
16. McCollom, T.M.; Seewald, J.S. Serpentinites, Hydrogen, and Life. *Elements* **2013**, *9*, 129–134. [\[CrossRef\]](#)
17. Blackburn, T.J.; Stockli, D.F.; Walker, J.D. Magnetite (U-Th)/He dating and its application to the geochronology of intermediate to mafic volcanic rocks. *Earth Planet. Sci. Lett.* **2007**, *259*, 360–371. [\[CrossRef\]](#)
18. Blackburn, T.J.; Stockli, D.F.; Carlson, R.W.; Berendsen, P. (U-Th)/He dating of kimberlites—A case study from north-eastern Kansas. *Earth Planet. Sci. Lett.* **2008**, *275*, 111–120. [\[CrossRef\]](#)
19. Cooperdock, E.H.; Stockli, D.F. Unraveling alteration histories in serpentinites and associated ultramafic rocks with magnetite (U-Th)/He geochronology. *Geology* **2016**, *44*, 967–970. [\[CrossRef\]](#)
20. Cooperdock, E.H.G.; Stockli, D.F.; Kelemen, P.B.; de Obeso, J.C. Timing of magnetite growth associated with peridotite-hosted carbonate veins in the SE Samail ophiolite, Wadi fins, Oman. *J. Geophys. Res. Solid Earth* **2020**, *125*, e2019JB018632. [\[CrossRef\]](#)
21. Schwartz, S.; Gautheron, C.; Ketcham, R.; Brunet, F.; Corre, M.; Agranier, A.; Pinna-Jamme, R.; Haurine, F.; Monvoin, G.; Riel, N. Unraveling the exhumation history of high-pressure ophiolites using magnetite (U-Th-Sm)/He thermochronometry. *Earth Planet. Sci. Lett.* **2020**, *543*, 116359. [\[CrossRef\]](#)
22. Lazar, C.; Cooperdock, E.H.G.; Seymour, B.H.T. A continental forearc serpentinite diapir with deep origins: Elemental signatures of slab-derived fluids and a mantle wedge protolith at New Idria, California. *Lithos* **2021**, *398–399*, 106252. [\[CrossRef\]](#)
23. Hofmann, F.; Cooperdock, E.H.G.; West, A.J.; Hildebrandt, D.; Strößner, K.; Farley, K.A. Exposure dating of detrital magnetite using ³He enabled by microCT and calibration of the cosmogenic ³He production rate in magnetite. *Geochronol. Discuss.* **2021**, *3*, 395–414. [\[CrossRef\]](#)
24. Gerin, C.; Gautheron, C.; Oliviero, E.; Bachelet, C.; Djimbi, D.M.; Seydoux-Guillaume, A.-M.; Tassan-Got, L.; Sarda, P.; Roques, J.; Garrido, F. Influence of vacancy damage on He diffusion in apatite investigated at atomic to mineralogical scales. *Geochim. Cosmoch. Acta* **2017**, *197*, 87–103. [\[CrossRef\]](#)
25. Gautheron, C.; Djimbi, D.M.; Roques, J.; Balout, H.; Ketcham, R.A.; Simoni, E.; Pik, R.; Seydoux-Guillaume, A.-M.; Tassan-Got, L. A multi-method, multi-scale theoretical study of He and Ne diffusion in zircon. *Geochim. Cosmoch. Acta* **2020**, *268*, 348–367. [\[CrossRef\]](#)
26. Djimbi, D.M.; Gautheron, C.; Roques, J.; Tassan-Got, L.; Gerin, C.; Simoni, E. Impact of apatite chemical composition on (U-Th)/He thermochronometry: An atomistic point of view. *Geochim. Et Cosmochim. Acta* **2015**, *167*, 162–176. [\[CrossRef\]](#)
27. Bassal, F.; Roques, J.; Gautheron, C. Neon diffusion in goethite, α -FeO(OH): A theoretical multi-scale study. *Phys. Chem. Miner.* **2020**, *47*, 14. [\[CrossRef\]](#)
28. Balout, H.; Roques, J.; Gautheron, C.; Tassan-Got, L.; Mbongo-Djimbi, D. Helium diffusion in pure hematite (α -Fe₂O₃) for thermochronometric applications: A theoretical multi-scale study. *Comput. Theor. Chem.* **2017**, *1099*, 21–28. [\[CrossRef\]](#)
29. Balout, H.; Roques, J.; Gautheron, C.; Tassan-Got, L. Computational investigation of the interstitial neon diffusion in pure hematite, α -Fe₂O₃. *Comput. Mater. Sci.* **2017**, *128*, 67–74. [\[CrossRef\]](#)
30. Hohenberg, P.; Kohn, W. Inhomogeneous Electron Gas. *Phys. Rev.* **1964**, *136*, B864–B871. [\[CrossRef\]](#)
31. Kohn, W.; Sham, L.J. Self-Consistent Equations Including Exchange and Correlation Effects. *Phys. Rev.* **1965**, *140*, A1133–A1138. [\[CrossRef\]](#)
32. Mills, G.; Jónsson, H.; Schenter, G.K. Reversible work transition state theory: Application to dissociative adsorption of hydrogen. *Surf. Sci.* **1995**, *324*, 305–337. [\[CrossRef\]](#)
33. Jónsson, H.; Mills, G.; Jacobsen, K.W. Nudged Elastic Band Method for Finding Minimum Energy Paths of Transitions. In *Classical and Quantum Dynamics in Condensed Phase Simulations*; Berne, J.B., Ciccotti, C., Coker, D.F., Eds.; World Scientific: Singapore, 1998; p. 385.
34. Fleet, M.E. The structure of magnetite. *Acta Crystallogr. Sect. B* **1981**, *37*, 917–920. [\[CrossRef\]](#)

35. Cornell, R.M.; Schwertmann, U. *The Iron Oxides: Structure, Properties, Reactions, Occurrences and Uses, Second Edition*; Wiley: Hoboken, NJ, USA, 2004.
36. Wright, J.P.; Attfield, J.P.; Radaelli, P.G. Charge ordered structure of magnetite Fe_3O_4 below the Verwey transition. *Phys. Rev. B* **2002**, *66*, 214422. [\[CrossRef\]](#)
37. Perdew, J.P.; Burke, K.; Ernzerhof, M. Generalized Gradient Approximation Made Simple. *Phys. Rev. Lett.* **1996**, *77*, 3865–3868. [\[CrossRef\]](#)
38. Blöchl, P.E. Projector augmented-wave method. *Phys. Rev. B* **1994**, *50*, 17953. [\[CrossRef\]](#) [\[PubMed\]](#)
39. Kresse, G.; Joubert, D. From ultrasoft pseudopotentials to the projector augmented-wave method. *Phys. Rev. B* **1999**, *59*, 1758–1775. [\[CrossRef\]](#)
40. Kresse, G.; Hafner, J. Ab initio molecular dynamics for open-shell transition metals. *Phys. Rev. B* **1994**, *48*, 13115. [\[CrossRef\]](#)
41. Kresse, G.; Furthmüller, J. Efficient iterative schemes for ab initio total-energy calculations using a plane-wave basis set. *Phys. Rev. B* **1996**, *54*, 11169. [\[CrossRef\]](#)
42. Guo, H.; Barnard, A.S. Thermodynamic modelling of nanomorphologies of hematite and goethite. *J. Mater. Chem.* **2011**, *21*, 11566–11577. [\[CrossRef\]](#)
43. Rohrbach, A.; Hafner, J.; Kresse, G. Electronic correlation effects in transition-metal sulfides. *J. Phys. Condens. Matter* **2003**, *15*, 979. [\[CrossRef\]](#)
44. Rollmann, G.; Rohrbach, A.; Entel, P.; Hafner, J. First-principles calculation of the structure and magnetic phases of hematite. *Physical Review B* **2004**, *69*, 165107. [\[CrossRef\]](#)
45. Yin, S.; Ellis, D.E. DFT studies of Cr(VI) complex adsorption on hydroxylated hematite (1102) surfaces. *Surf. Sci.* **2009**, *603*, 736–746. [\[CrossRef\]](#)
46. Dudarev, S.L.; Liechtenstein, A.I.; Castell, M.R.; Briggs, G.A.D.; Sutton, A.P. Surface states on NiO (100) and the origin of the contrast reversal in atomically resolved scanning tunneling microscope images. *Phys. Rev. B* **1997**, *56*, 4900–4908. [\[CrossRef\]](#)
47. Roldan, A.; Santos-Carballal, D.; de Leeuw, N.H. A comparative DFT study of the mechanical and electronic properties of greigite Fe_3S_4 and magnetite Fe_3O_4 . *J. Chem. Phys.* **2013**, *138*, 204712. [\[CrossRef\]](#) [\[PubMed\]](#)
48. Santos-Carballal, D.; Roldan, A.; Grau-Crespo, R.; de Leeuw, N.H. A DFT study of the structures, stabilities and redox behaviour of the major surfaces of magnetite Fe_3O_4 . *Chem. Phys.* **2014**, *16*, 21082–21097. [\[CrossRef\]](#)
49. Monkhorst, H.J.; Pack, J.D. Special points for Brillouin-zone integrations. *Phys. Rev. B* **1976**, *13*, 5188–5192. [\[CrossRef\]](#)
50. Bortz, A.B.; Kalos, M.H.; Lebowitz, J.L. A new algorithm for Monte Carlo simulation of Ising spin systems. *J. Comput. Phys.* **1975**, *17*, 10–18. [\[CrossRef\]](#)
51. Einstein, A. Über die von der molekularkinetischen Theorie der Wärme geforderte Bewegung von in ruhenden Flüssigkeiten suspendierten Teilchen. *Ann. Phys.* **1905**, *322*, 549–560. [\[CrossRef\]](#)
52. Ziegler, J.F. *Helium Stopping Powers and Ranges in All Elements*; Pergamon Press: Oxford, UK, 1977; Volume 4.
53. Ziegler, J.F. *SRIM-2008 The Stopping Range of Ions in Matter*; United States Naval Academy: Annapolis, MD, USA, 2008.
54. Dodson, M.H. Closure temperature in cooling geochronological and petrological systems. *Contrib. Mineral. Petrol.* **1973**, *40*, 259–274. [\[CrossRef\]](#)
55. Recanati, A.; Gautheron, C.; Barbarand, J.; Missenard, B.; Pinna-Jamme, R.; Tassan-Got, L.; Carter, A.; Douville, E.; Bordier, L.; Pagel, M.; et al. Helium trapping in apatite damage: Insights from (U-Th-Sm)/He dating of different granitoid lithologies. *Chem. Geol.* **2017**, *470*, 116–131. [\[CrossRef\]](#)
56. Shuster, D.; Flowers, R.; Farley, K.A. The influence of natural radiation damage on helium diffusion kinetics in apatite. *Earth Planet. Sci. Lett.* **2006**, *249*, 148–161. [\[CrossRef\]](#)
57. Farley, K.A. Helium diffusion from apatite: General behavior as illustrated by Durango fluorapatite. *J. Geophys. Res.* **2000**, *105*, 2903–2914. [\[CrossRef\]](#)
58. Hallström, S.; Höglund, L.; Ågren, J. Modeling of iron diffusion in the iron oxides magnetite and hematite with variable stoichiometry. *Acta Mater.* **2011**, *59*, 53–60. [\[CrossRef\]](#)
59. Sundman, B. An assessment of the Fe-O system. *J. Phase Equilibria* **1991**, *12*, 127–140. [\[CrossRef\]](#)
60. Dieckmann, R. Defects and Cation Diffusion in Magnetite (IV): Nonstoichiometry and Point Defect Structure of Magnetite ($\text{Fe}_3\text{-}\delta\text{O}_4$). *Ber. Der Bunsenges. Für Phys. Chem.* **1982**, *86*, 112–118. [\[CrossRef\]](#)
61. Arras, R.; Warot-Fonrose, B.; Calmels, L. Electronic structure near cationic defects in magnetite. *J. Phys. Condens. Matter* **2013**, *25*, 256002. [\[CrossRef\]](#)
62. Xu, H.; Shen, Z.; Konishi, H. Si-magnetite nano-precipitates in silician magnetite from banded iron formation: Z-contrast imaging and ab initio study. *Am. Mineral.* **2014**, *99*, 2196–2202. [\[CrossRef\]](#)
63. Bender, W.M.; Becker, U. Quantum-Mechanical Investigation of the Structures and Energetics of Uranium and Plutonium Incorporated into the Magnetite (Fe_3O_4) Lattice. *ACS Earth Space Chem.* **2019**, *3*, 637–651. [\[CrossRef\]](#)